Check for updates

NANO · MICRO small
www.small-journal.com

Non-Aqueous Electrochemical CO_2 Reduction to Multivariate C_2-Products Over Single Atom Catalyst at Current Density up to 100 mA cm^{-2}

*Rajan R. Bhawnani, Rohan Sartape, Vamsi V Gande, Michael L. Barsoum, Elias M. Kallon, Roberto dos Reis, Vinayak P. Dravid, and Meenesh R. Singh**

Electrochemical CO_2 reduction reaction (CO_2-RR) in non-aqueous electrolytes offers significant advantages over aqueous systems, as it boosts CO_2 solubility and limits the formation of HCO_3^- and CO_3^{2-} anions. Metal–organic frameworks (MOFs) in non-aqueous CO_2-RR makes an attractive system for CO_2 capture and conversion. However, the predominantly organic composition of MOFs limits their electrical conductivity and stability in electrocatalysis, where they suffer from electrolytic decomposition. In this work, electrically conductive and stable Zirconium (Zr)-based porphyrin MOF, specifically PCN-222, metalated with a single-atom Cu has been explored, which serves as an efficient single-atom catalyst (SAC) for CO_2-RR. PCN- 222(Cu) demonstrates a substantial enhancement in redox activity due to the synergistic effect of the Zr matrix and the single-atom Cu site, facilitating complete reduction of C_2 species under non-aqueous electrolytic conditions. The current densities achieved (≈100 mA cm^{-2}) are 4–5 times higher than previously reported values for MOFs, with a faradaic efficiency of up to 40% for acetate production, along with other multivariate C_2 products, which have never been achieved previously in non-aqueous systems. Characterization using X-ray and various spectroscopic techniques, reveals critical insights into the role of the Zr matrix and Cu sites in CO_2 reduction, benchmarking PCN-222(Cu) for MOF-based SAC electrocatalysis.

1. Introduction

Electrocatalytic reduction of CO_2 has been one of the prime areas of research in the field of sustainable chemistry and engineering.[1–4] Due to the increase in average global temperature annually, there has been an equivalent surge in developing processes that can efficiently capture and convert CO_2 into value-added products and fuels.[5–7] In the past two decades, advancements have been made in identifying metallic and molecular catalysts and testing them for efficient electrocatalytic reduction to syngas, C_1 (methane, methanol, formic acid), and C_2 (ethylene, ethanol, acetic acid, etc.) products.[8–11] To enhance the catalyst performance in terms of selectivity and scalable current densities, properties like surface area and binding efficiency of the gaseous species and intermediates on the catalyst surface play a key role.[12–14] Therefore, taking these into consideration, the field of materials research has primarily focused on engineering catalysts in the form of nanofibers, nanoparticles, 2D nanorods, etc. that have not only increased performance but also provided longer operational stability.[15–19]

In conjunction with catalyst performance, efforts have also been made to develop processes to maximize selectivity toward a variety of C_1- and C_2-products and reduce the unwanted hydrogen evolution reaction (HER).[20,21] For example, deploying Cu alloys with small quantities of Zn, Ag, Sb, and Sn has enhanced the selectivity of ethanol and ethylene, thereby

R. R. Bhawnani, R. Sartape, V. V. Gande, M. R. Singh
Department of Chemical Engineering
University of Illinois Chicago
Chicago, IL 60607, USA
E-mail: mrsingh@uic.edu

The ORCID identification number(s) for the author(s) of this article can be found under https://doi.org/10.1002/smll.202408010

© 2024 The Author(s). Small published by Wiley-VCH GmbH. This is an open access article under the terms of the Creative Commons Attribution-NonCommercial-NoDerivs License, which permits use and distribution in any medium, provided the original work is properly cited, the use is non-commercial and no modifications or adaptations are made.

DOI: 10.1002/smll.202408010

M. L. Barsoum, E. M. Kallon, R. dos Reis, V. P. Dravid
Department of Materials Science & Engineering
Northwestern University
Evanston, IL 60208, USA

R. dos Reis, V. P. Dravid
International Institute of Nanotechnology
Northwestern University
Evanston, IL 60208, USA

R. dos Reis, V. P. Dravid
The NUANCE Center
Northwestern University
Evanston, IL 60208, USA

minimizing parasitic H_2 formation.[22–27] Studies have also been conducted where the catalyst is coated with thin layers of ionomers to make the surface marginally hydrophobic to inhibit HER without compromising the binding of CO_2 and other intermediates on the catalyst surface.[28–31] Along with these strategies, performing the CO_2-RR reaction in non-aqueous environments has also proven to be one of the propitious approaches toward tackling HER.[32–35] The solubility of CO_2 in non-aqueous environments is much higher compared to aqueous electrolytes. Furthermore, non-aqueous conditions allow tunable control of proton sources for the reduction of CO_2 to valuable products like formates, oxalates, malates, glycolates, and glyoxalates.[36–41] However, the reported Faradaic Efficiencies (FEs) for C_2-products in non-aqueous media have generally been lower, with the majority of selectivity favoring CO production. This is applicable for metallic as well as certain molecular catalysts that have been reported previously. Additionally, the obtained current densities have been on the lower end, posing further challenges for commercializing and scaling up the process in a non-aqueous medium. Therefore, there is a need for the development of effective catalysts that provide higher FEs for C_2-products alongside higher current densities in a non-aqueous medium.

Discovery and development of Metal–Organic Frameworks (MOFs) have showcased exceptional CO_2 capture and separation due to their high porosities and affinity toward select gases.[42–45] Most MOFs have very low electrical conductivities making them poor candidates for electrocatalytic applications.[46,47] However, a few classes of MOFs, including Porphyrin Coordination Networks (PCNs), have emerged to provide comparable performance to the metallic catalysts in this area for electrocatalytic and photocatalytic CO_2 reduction.[48] Metalated derivates of PCN-222, one of the Zr-based porphyrinic frameworks, have been developed and studied for CO_2 reduction reaction (CO_2-RR).[49–51] In aqueous environments, Cu-metalated PCN-222 yielded ethylene (25% FE) whereas, in a non-aqueous medium Fe-metalated MOF-525 (a polymorph of PCN-222) yielded CO (up to 45% FE).[50,51] The metalated sites act as single-atom catalysts, which have proven to significantly increase the overall selectivity toward valuable products and yields and minimize the HER.[52–54] MOF-stabilized single atom sites in non-aqueous environments further control the proton addition to the reaction intermediates and products and allow a greater extent of reduction. It has also been reported that the single atom sites of CO_2RR catalysts such as Cu have exhibited altered density of states that further manipulates the coordination environments to improve intermediates binding and coupling reactions.[55–57]

In this work, we report the electrochemical CO_2-RR in a continuous flow cell system with PCN-222(Cu) as the catalyst in non-aqueous media. PCN-222 (Cu), as seen in **Figure 1a**, has a *csq* topology with a hexagonal P6mmm space group. The porphyrinic center is metalated with a single Cu atom, and the Zr-porphyrin network acts as an effective medium for electron transport (Figure 1b). Moreover, the Zr_6 nodes provide exceptional chemical stability and, in conjunction with the single-atom Cu sites, are responsible for the high current densities of up to 90 mA cm^{-2} at -2.4 V versus Ag/AgCl. As a non-aqueous electrolyte, tetrabutylammonium hexafluorophosphate ($TBAPF_6$) was dissolved in acetonitrile (ACN) to serve as a catholyte. The anolyte was 0.5 M H_2SO_4, and both chambers were separated by a cathode exchange membrane. Due to the aqueous nature of the anolyte, small amounts of water molecules diffuse into the catholyte chamber as a function of time, which aids the formation of protonated C_2 -products in the catholyte chamber. The acidic environment in the catholyte chamber due to the $TBAPF_6$ salt, the -OH and the -H_2O ligands on the Zr_6 node of the MOF get deprotonated that further facilitates complete reduction of the C_2 product species. Acetate was the primary product obtained in this study with FE upto 40% at -2.3 V versus Ag/AgCl, which is a resultant of a complete reduction of other C_2 products like oxalate, glyoxalate, and glycolate. Additionally, formic acid and CO were also obtained with FEs between 15–25%. **Figure 2a** shows the previously reported catalysts (metallic and molecular) and their corresponding FEs and the current densities in non-aqueous environments and have been compared against this work. A handful of studies have reported the formation of acetates as the major product in non-aqueous conditions. Figure 2b shows the comparison plot of studies that have reported acetic acid/acetate as the main product in both aqueous and non-aqueous environments. Except for this work, all the previous studies in Figure 2b have been conducted in aqueous environments. It can be seen that the performance reported in this work under non-aqueous conditions is comparable to that of the reported aqueous studies. Detailed comparison of C_1- and C_2-products is also included in Tables S1 and S2 (Supporting Information). Along with the performance, the pathways of formation of each of the products obtained have also been illustrated toward the conclusive portion of this study.

2. Results and Discussion

2.1. Catalyst Synthesis and Characterization

Solvothermal routes were implemented to synthesize PCN-222 and Cu-metalated PCN-222. Detailed synthesis protocol is included in Section S1 (Supporting Information). Post-metalation of PCN-222 in the presence of $CuCl_2$ was performed to metalate the porphyrin centers of the MOF.[77–80] Powder X-ray diffraction (PXRD) signatures of synthesized non-metalated and metalated bulk PCN-222 are shown in **Figure 3a**. The experimental signatures are in good agreement with the simulated spectra of PCN-222. Further, Fourier-Transformed Infrared (FTIR) and Ultraviolet (UV) spectroscopy were carried out to confirm the PCN-222 signature and Cu coordination at the porphyrin centers, respectively. Figure 3b shows the FTIR spectra of PCN-222 and PCN-222(Cu). The peaks at 1655, 1384, and 1285 cm^{-1} represent -C═O, -C═C-, and -C—O bonds, respectively, as reported previously.[81–83] UV spectroscopy was performed by digesting the individual bulk powders in 1 M NaOH, as reported previously.[51,77] UV analysis not only provides a confirmation of the Cu coordination but also provides a qualitative measurement of the complete metalation of the porphyrin centers. As seen in Figure 3c, the non-metalated TCPP and PCN-222 have similar locations of the Q-bands at 527, 566, and 597nm. In the case of Cu-metalated PCN-222, only two of the three Q-bands are seen, and more importantly, they appear to be shifted when compared to their non-metalated analogues. This further confirms the complete metalation of the porphyrin centers with the Cu atom, and the observation is in line with the previous reports. The TCPP and TCPP(Cu) act as fingerprint spectra to confirm the

© 2024 The Author(s). Small published by Wiley-VCH GmbH

16136829, 0, Downloaded from https://onlinelibrary.wiley.com/doi/10.1002/smll.202408010 by University Of Illinois, Wiley Online Library on [29/01/2025]. See the Terms and Conditions (https://onlinelibrary.wiley.com/terms-and-conditions) on Wiley Online Library for rules of use; OA articles are governed by the applicable Creative Commons License

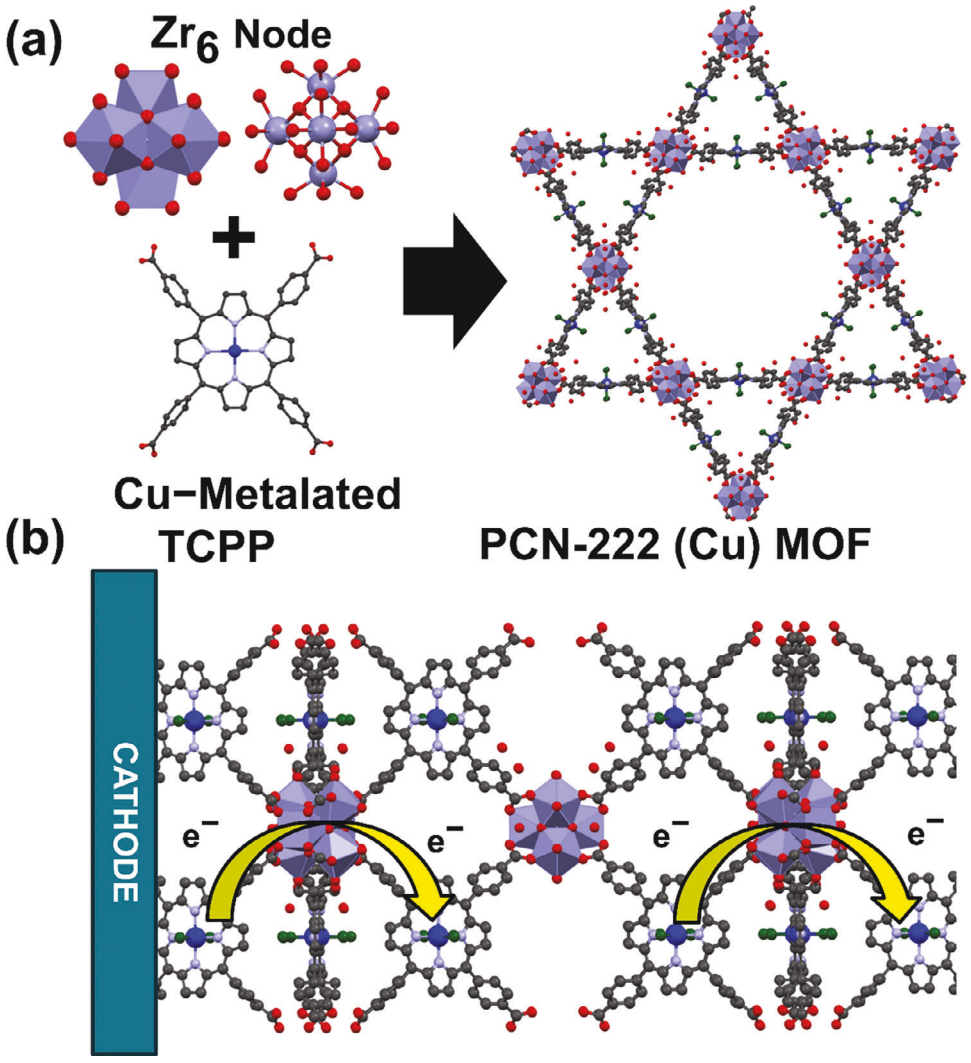

Figure 1. a) Zr_6 nodes and Cu-metalated Tetrakis (-4-carboxyphenyl) porphyrin (TCPP) linker forming the 8-connected, csq topology PCN-222(Cu) MOF, b) PCN-222(Cu) MOF deposited on a GDE cathode for CO_2 electroreduction showing electron transport through the redox-conductive TCPP linker, between the single atom Cu sites. H-atoms have not been shown for clarity purposes.

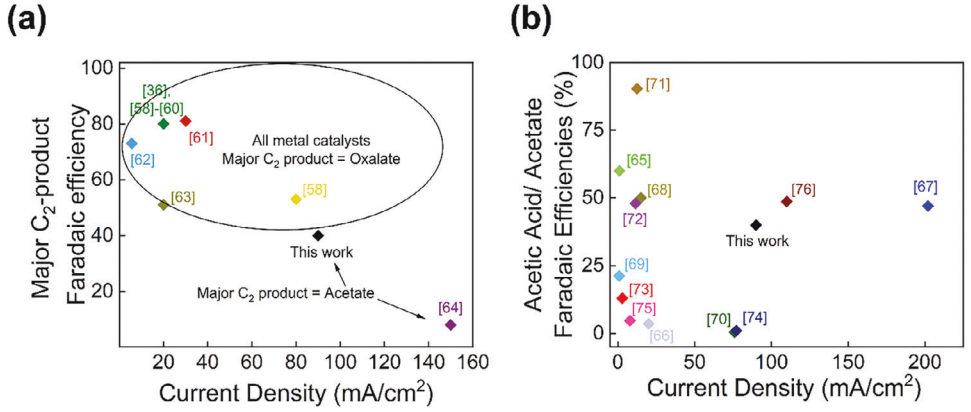

Figure 2. a) Comparison of performance (FE vs current densities) of previously reported catalysts in non-aqueous environments. The referenced articles are: ref. [36,58–64] b) Previously reported performance of different catalysts for electroreduction of CO_2 to Acetic acid/Acetate. Except for this work, all the previous studies marked here have been conducted in aqueous environments. The referenced articles are: ref. [65–76].

© 2024 The Author(s). Small published by Wiley-VCH GmbH

16136829, 0, Downloaded from https://onlinelibrary.wiley.com/doi/10.1002/smll.202408010 by University Of Illinois, Wiley Online Library on [29/01/2025]. See the Terms and Conditions (https://onlinelibrary.wiley.com/terms-and-conditions) on Wiley Online Library for rules of use; OA articles are governed by the applicable Creative Commons License

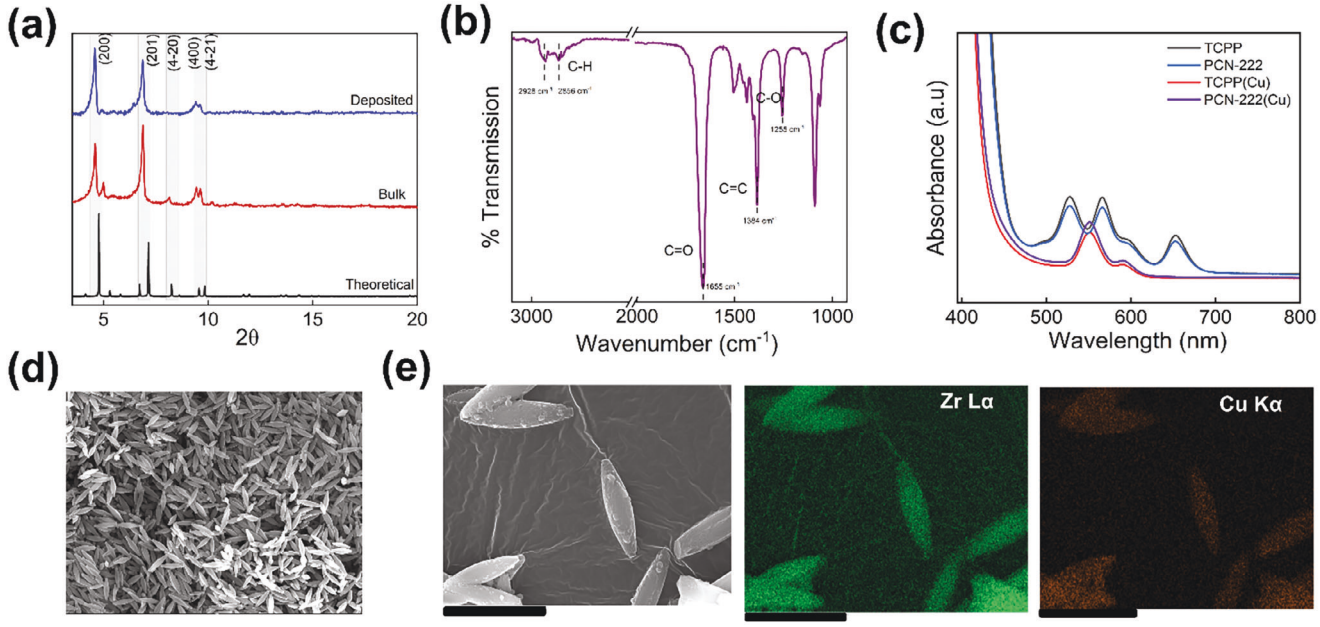

Figure 3. a) Simulated, powder (bulk) and deposited (on GDE) XRD spectra of PCN-222(Cu). Upon deposition, the PCN-222(Cu) MOF retains their crystal structure, b) FTIR spectra of PCN-222(Cu) deposition on GDE, c) UV spectra of non-metalated and metalated TCPP and PCN-222 MOF confirming the single atom metalation of Cu in the porphyrin cage. Equal amounts of all powders were digested in 2 mL of 1 M NaOH and the samples were analyzed on a UV spectrometer, d) SEM image of deposition of PCN-222(Cu) on GDE, e) SEM-EDS of bulk PCN-222(Cu) with Zr and Cu elemental maps. The scale bar for all images is 5 μm.

metalation in their respective PCN derivatives. Scanning-electron microscopy coupled with energy dispersive X- ray spectroscopy (SEM-EDS) analysis was performed on the bulk powder and the MOF deposited on the gas diffusion electrode (GDE) to further confirm the presence of Cu. Figure 3d shows the typical ellipsoidal morphology of the PCN-222(Cu) MOF deposited on the GDE. Figure 3e,f confirms the presence of the Zr and Cu, respectively, through the EDS analysis of single crystal MOF. Inductively Coupled Plasma Mass Spectrometry (ICP-MS) analysis was performed to confirm the weight percentages of Zr and Cu in the bulk PCN-222(Cu) powder. The obtained percentages were in agreement with the theoretical elemental weight percentages in the PCN-222(Cu) MOF. The results of the supplementary information are tabulated in Table S3 (Supporting Information). The details of the synthesis of the catalyst ink are reported in Section S1 (Supporting Information) of the supplementary information. The P-XRD, FTIR, and SEM analyses were repeated on the MOF ink-coated GDEs to ensure successful deposition and signature of the deposited MOF. The obtained results exactly matched the results obtained from the bulk PCN-222(Cu) analysis. The experimental and simulated XRD spectra and the SEM of the PCN-222 only depositions that were used for control studies are included as Figures S1 and S2 (Supporting Information). Scanning transmission electron microscopy coupled with EDS (STEM-EDS) analysis was performed on the bulk PCN-222(Cu) MOF to obtain the low and high-resolution images and the elemental distribution. **Figure** 4a,b shows the low-resolution STEM-EDS image of single crystal PCN-222(Cu) MOF. Figure 4c,d shows high-resolution STEM-EDS of edges of one of the PCN-222(Cu) crystals. Conclusively Figure 4 confirms the distribution of Zr and Cu at the lattice scale. The EDS spectrum and the d-spacing of the (001) face obtained from the STEM experiments are included in Figures S1 and S2 (Supporting Information).

2.2. Electrochemical Reduction of CO_2 in Non-Aqueous Media

All electrochemical reduction experiments were conducted in a continuous, flow cell-based setup similar to the one reported previously that utilized aqueous electrolytes with slight modifications.[84–86] The schematic of a 3D-printed electrochemical cell is shown in **Figure** 5a. The anolyte chamber was filled with 0.5 M H_2SO_4 and was maintained without recirculation. On the other hand, the catholyte chamber was recirculated with a 0.5 M $TBAPF_6$ acetonitrile electrolyte solution as shown in Figure 5b. Both chambers were separated by a Cation Exchange Membrane (CEM). The setup was configured with a standard three-electrode configuration containing the PCN-222(Cu) film on GDE, an Ag/AgCl electrode, and a Pt ingot, that acts as working, reference, and counter electrodes, respectively. Prior to conducting the electrochemical reduction experiments, linear sweep voltammetry (LSV) measurements were conducted with Ar-saturated and CO_2-saturated electrolyte solutions. As seen in Figure 5c, an increase in the currents beyond -1.4 V versus Ag/AgCl for the CO_2 saturated solution, indicates the activity of the catalyst toward reduction of CO_2.

The FEs for liquid and gaseous products were obtained from the high-performance liquid chromatography (HPLC) and gas chromatography (GC) analysis, respectively (details in Section S2, Supporting Information). Figure 5d shows the product distributions and the corresponding current densities at different

© 2024 The Author(s). Small published by Wiley-VCH GmbH

16136829, 0, Downloaded from https://onlinelibrary.wiley.com/doi/10.1002/smll.202408010 by University Of Illinois, Wiley Online Library on [29/01/2025]. See the Terms and Conditions (https://onlinelibrary.wiley.com/terms-and-conditions) on Wiley Online Library for rules of use; OA articles are governed by the applicable Creative Commons License

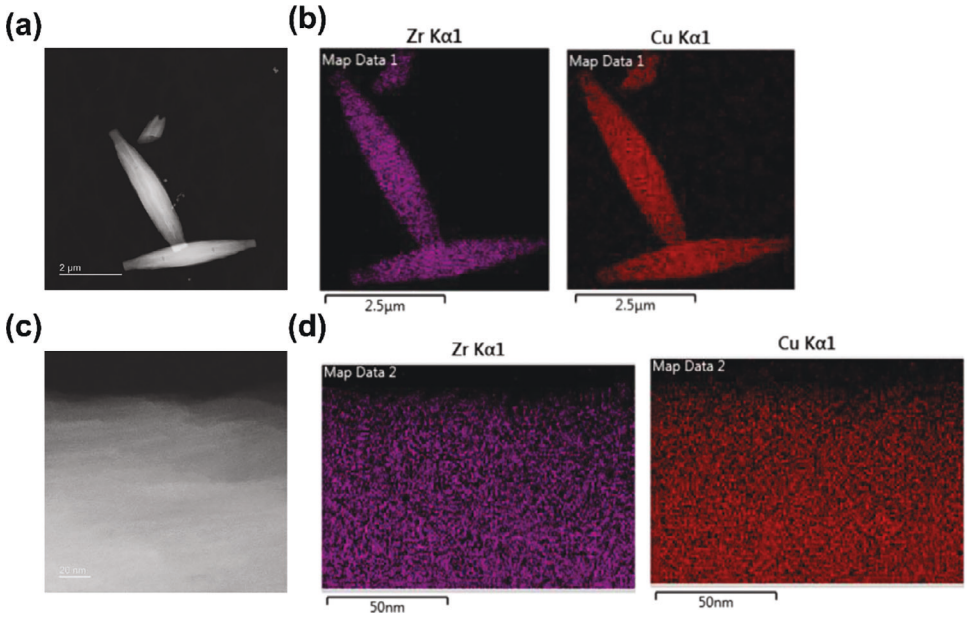

Figure 4. (a) STEM image of single crystals of PCN-222(Cu), scale bar is 2 μm, b) STEM-EDS mapping of image in (a) single crystals of PCN-222(Cu) showing Zr and Cu signature, scale bar is 2.5 μm, c) High-resolution STEM image of PCN-222(Cu), scale bar is 20 nm, (d) High-resolution STEM-EDS mapping of image in c) sample showing lattice level resolution of Zr and Cu distribution, scale bar is 50nm. The EDS spectrum and lattice fringes showing d-spacing of the (100) face for the STEM-EDS have been included in Figures S3 and S4 (Supporting Information).

potentials versus Ag/AgCl at which the electroreduction experiments were conducted. At lower potentials, i.e., at -1.8 V versus Ag/AgCl, the product stream was dominated by H_2 at 46% FE followed by 15% CO as the main gaseous products and smaller percentages of liquid products were detected, with the majority of it being acetate at 12%. However, as the reduction potential increased, the FE of acetate increased up to 40% at -2.3 V versus Ag/AgCl. CO was also observed at a high % along with other liquid products like oxalate, glycolate, glyoxylate, and formate at lower percentages. However, the product selectivity toward acetate drops when the potential is increased beyond -2.3 V versus Ag/AgCl. At higher potentials, a slightly higher percentage of oxalate was observed along with H_2 and CO with less than 3% of the C_2 products each. The control experiments to test the performance of PCN-222 only in the absence of Cu were conducted and the obtained LSVs, product distributions and current densities are included as Figure S5 and S6 (Supporting Information). Ex situ FTIR analysis was conducted to study the liquid products at different timestamps. The samples were collected from the recirculating reservoirs at different times during the reduction reaction at -2.3 V versus Ag/AgCl and were analyzed under FTIR. Prior to analysis, the background spectra were subtracted with the CO_2-saturated pure electrolyte solution at t = 0 to detect the signal from the product species. The peaks at 1702 and 1635 cm^{-1} shown in Figure 5e correspond to the -COO asymmetric stretches, whereas the peak at 1375 cm^{-1} shown in Figure 5f corresponds to the -COO symmetric stretch.[61] Due to the -COO bond being a common functional group in all the obtained products, the individual product presence cannot be distinguished. However, LC analysis of these exact samples confirmed the presence of these multivariate products shown in Figure 5d. The presence of protonated products in the stream (Formate, Glycolate, Glyoxylate, and Acetate) can be directly attributed to the presence of protons in the catholyte chamber. One of the primary reasons for the presence of H^+ ions can be attributed to the migration/diffusion of water molecules from the acidic anolyte to the catholyte chamber through the CEM membrane. This hypothesis has been reported previously in cases where the anolyte contained protic electrolytic solutions, which further justifies the presence of H_2 in the gaseous stream due to some HER occurring at the cathode suppressing CO_2 reduction.[33,34,87] Figure 5g further shows the increase in the -OH stretch intensities. This signal can be attributed to either the presence of water or from the formation of -COO species in the product stream. To further investigate the increase in the -OH signal, Karl-Fisher (KF) titrations on these samples from different timestamps were performed. These titrations did further confirm the presence of water in the product samples, thereby confirming the reason for the increase in -OH peak intensities in FTIR. The increasing weight percentages of water obtained from the titrations at different times are shown in Figure 5h.

2.3. Role of the Catalyst and Reaction Mechanism of Multivariate C_2-Products Formation

2.3.1. Role of PCN-222(Cu) Catalyst

The presence of H^+ ions and H_2O molecules is crucial for the reaction progression to these valuable C_2 products. One of the scenarios of the presence of water molecules is due to the migration from the anolyte chamber through the membrane (Figure 3h). On the other hand, in the case of the catholyte, TBAPF6 is an acidic electrolyte that maintains the pKa of the medium in the

© 2024 The Author(s). Small published by Wiley-VCH GmbH

16136829, 0, Downloaded from https://onlinelibrary.wiley.com/doi/10.1002/smll.202408010 by University Of Illinois, Wiley Online Library on [29/01/2025]. See the Terms and Conditions (https://onlinelibrary.wiley.com/terms-and-conditions) on Wiley Online Library for rules of use; OA articles are governed by the applicable Creative Commons License

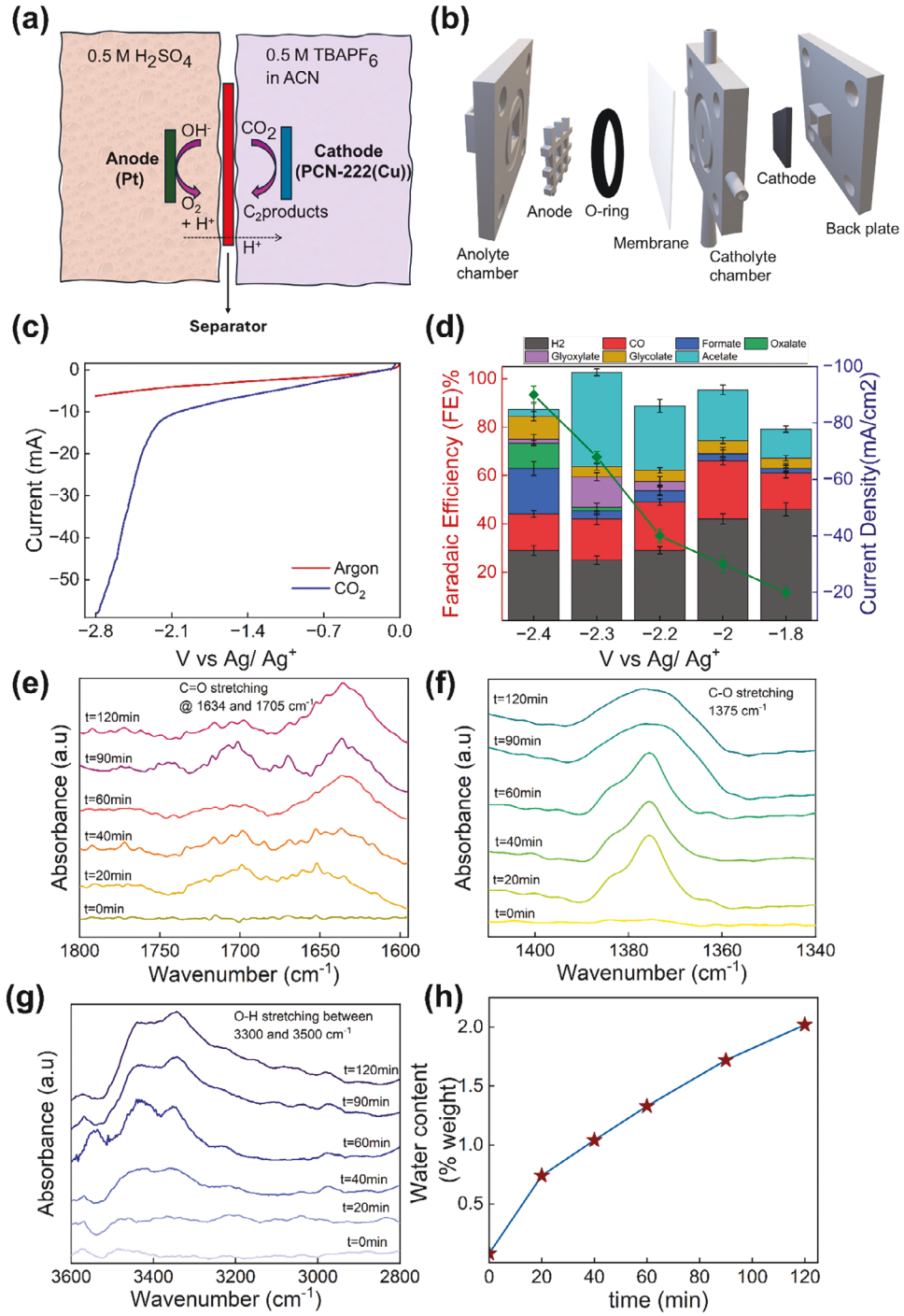

Figure 5. a) Schematic representation of the continuous flow setup for electrochemical CO_2-RR studies, b) 3D view of the individual parts of the flow cell assembly, c) Linear Sweep voltammogram (LSV) of PCN-222(Cu) MOF in 0.5 M $TBAPF_6$ in acetonitrile with Pt counter electrode and Ag/AgCl reference in Ar and CO_2 environments respectively, depicting the activity of the catalyst toward CO_2 reduction, d) Faradaic efficiencies and current densities for CO_2-RR using the PCN-222(Cu) catalyst against different potentials versus Ag/AgCl electrode, e) Ex situ FTIR analysis of the product solution showing the -C═O stretching at 1634 and 1705 cm^{-1} that can be attributed to the signatures of oxalate, glyoxalate, glycolate and acetate, f) Ex situ FTIR analysis of the product solution showing the -C—O stretching at 1375 cm^{-1} that can be attributed to the signatures of oxalate, glyoxalate, glycolate and acetate, g) -O—H signature in the product solution from ex situ FTIR attributed to migrated water from the anolyte to the catholyte, h) Karl–Fisher (KF) titrations to obtain the weight% of migrated water from the anolyte to the catholyte.

© 2024 The Author(s). Small published by Wiley-VCH GmbH

16136829, 0, Downloaded from https://onlinelibrary.wiley.com/doi/10.1002/smll.202408010 by University Of Illinois, Wiley Online Library on [29/01/2025]. See the Terms and Conditions (https://onlinelibrary.wiley.com/terms-and-conditions) on Wiley Online Library for rules of use; OA articles are governed by the applicable Creative Commons License

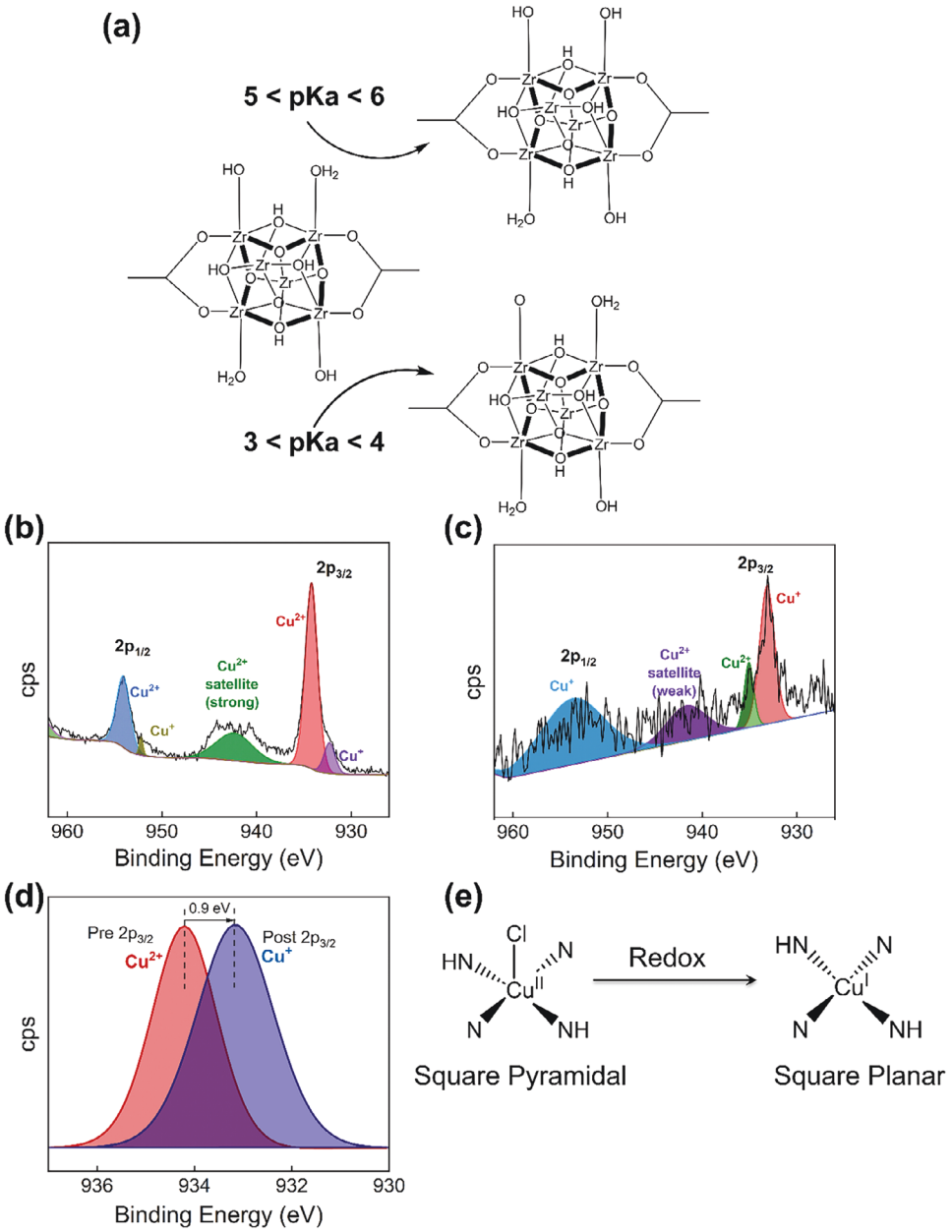

Figure 6. a) Zr_6 node showing the proton topology of -OH and -H_2O ligands and the deprotonation of these ligands and different pKas, b) High-resolution XPS spectra of Cu from the PCN-222(Cu) deposition pre-electrolysis, c) High-resolution XPS spectra of Cu from the PCN-222(Cu) deposition post-electrolysis, d) Comparison of the $2p_{3/2}$ peaks of Cu from (b) and (c) showing the shift in the binding energies implying the change in oxidation state of Cu from Cu-(II) to Cu-(I), e) Possible structural transformation and coordination environments of Cu in the porphyrin cage pre- and post- electrolysis.

range of 3.5–6 in acetonitrile.[88,89] The PCN-222 consists of the 8-COO-connected polynuclear Zr nodes in which the remainder of the coordination environment of the polynuclear core is satisfied by -OH and -H_2O ligands. These water and hydroxyl groups are responsible for the Bronsted acidity of the molecular catalyst.[90] From previous potentiometric acid–base titration studies of Zr MOFs and computational pKa calculations, it was observed that in the mentioned pKa range, these hydroxyl and water ligands dissociate to release protons.[81,90–92] These two combined scenarios justify the availability of the protons for reaction progression in the catholyte chamber. **Figure 6a** shows the topology of the Zr node and the pKa ranges at which the protons are released in the solution from previous reports. Therefore, it can be stated that the catholyte environment is moderately acidic that also determines the dominant reaction pathways for CO_2 reduction.

The reaction proceeds with the sequential addition of H^+ and e^- to the dianionic species present in the catholyte chamber (discussed in the next section). The Cu-II site is reduced to Cu-I, therefore acting as the electron donor for the reduction reactions. X-ray photoelectron spectroscopy (XPS) analysis of pre- and

© 2024 The Author(s). Small published by Wiley-VCH GmbH

16136829, 0, Downloaded from https://onlinelibrary.wiley.com/doi/10.1002/smll.202408010 by University Of Illinois, Wiley Online Library on [29/01/2025]. See the Terms and Conditions (https://onlinelibrary.wiley.com/terms-and-conditions) on Wiley Online Library for rules of use; OA articles are governed by the applicable Creative Commons License

post-electrocatalysis samples confirms the transition from the Cu-II oxidation state to Cu-I oxidation state. Figure 6b–d shows the pre-, post- and comparison of the $2p_{3/2}$ peak location for the ionic Cu species. The metalation of the porphyrin compounds is usually performed in presence of metal halides, in this case $CuCl_2$. The final coordination of Cu in the porphyrin cage is such that the one of the -Cl remains bonded to the Cu and the electron donor N-groups in the porphyrin cage, form a coordinate bond with the central Cu-atom. Thus, the final molecular configuration of the metalated Cu-II is square pyramidal. By application of the reduction potential, the electron hopping mechanism and reduction of the single atom Cu-sites alters the coordination environment and thus its molecular configuration inside the cage. Thus, as seen in Figure 6e, the final molecular geometry of the Cu is transformed into the square-planar structure. This phenomenon has been hypothesized in previous studies under similar circumstances.[93] Further post-electrolysis characterizations such as XRD, SEM and XPS are included as Figures S7–S9 (Supporting Information) respectively in the supplementary information.

2.3.2. Reaction Mechanism

As discussed above, the availability of the protons and electrons is governed by the nature of the catalyst. However, the extent of the reduction reaction is mainly governed by the overpotential. In other words, the overpotential determines the rate at which the electrons and protons get added to a variety of species occurring on different pathways on the energy landscape. The electrochemical reaction initiates with the adsorption of the CO_2 molecule on the Cu single-atom site, which forms a highly reactive CO_2 radical anion (CO_2^{-*}). All the reaction pathways proceed hereafter, as shown in **Figure 7**. Figure 7 (Scheme 1) shows the pathways for the formation of CO and HCO_3^-. To stabilize this radical, a nucleophilic disproportionation reaction takes place, which in the presence of 1 H^+ and 1 e^- yields CO and HCO_3^-. Figure 7 (Scheme 2) shows a competitive reaction to the one shown in Figure 7 (Scheme 1), leading to the formation of formate, where the radical anion is simply stabilized by an addition of H^+ and e^-. Higher FE for CO is obtained compared to $HCOO^-$ due to the limited availability of protons in the non-aqueous medium; thus, the disproportionation reaction is dominant. Moving forward, Figure 7 (Scheme 3) shows the formation of the oxalate ion, which is a result of dimerization occurring between two CO_2^{-*} radical anions, which is the most favored pathway for radical stabilization. This leads to the formation of anionic oxalate molecules. In moderately acidic environments, the protonation of oxalate molecules is favored leading to further reduction and rearrangement of protons to form the hydrated glyoxylate molecule. Each of the further reduction steps: 1) glyoxylate to glycolate and 2) glycolate to acetate follow the traditional e H e H mechanism as shown in Figure 7 (Scheme 4). Since the formation of glycolate and acetate initiates from glyoxyalate, the overall reaction is limited by the dehydration step of the glyoxalate molecule. However, the forward reaction is favored as the dehydration is favored by the acidic environment in the catholyte chamber. The resultant aldehyde intermediate is essential for the formation of reduced species – glycolate and acetate.

3. Conclusion

The synthesis and detailed study of the Cu-metalated PCN-222 MOF, presented here, have led to a significant step forward in CO_2 electroreduction, especially in non-aqueous environments. By successfully adding single-atom Cu into the porphyrin centers of PCN-222, we created a catalyst that not only remains stable during use but also shows much higher activity compared to previous MOFs, achieving current densities up to five times greater. Importantly, this catalyst is highly selective for producing valuable C2 products like acetate, with a Faradaic efficiency of up to 40%. This high performance is due to the effective interaction between the Zr matrix and the Cu active sites, which supports efficient electron transfer and proton availability, helping to drive the CO_2 reduction process.

The analysis of the reaction mechanisms, supported by XPS studies, shows that the Cu sites play a crucial role in stabilizing reaction intermediates and facilitating the reduction process by changing their oxidation state. The moderate acidity in the reaction environment also contributes to the catalyst's high selectivity and efficiency.

Overall, this work sets a new standard for MOF-based catalysts and offers a promising approach for developing efficient, scalable technologies for CO_2 conversion. The strong experimental results and clear understanding of the reaction mechanisms suggest that PCN-222(Cu) could play a key role in future efforts to reduce carbon emissions and create valuable chemical products from CO_2.

4. Experimental Section

Synthesis of PCN-222 (Cu) MOF and Electrode Fabrication: *PCN-222(Cu) Synthesis*: Detailed synthesis protocol and electrode preparation are included in Section S1 (Supporting Information). A traditional solvothermal method was used to synthesize PCN-222. $ZrOCl_2.8H_2O$ (30mg), TCPP (10mg), and Benzoic acid (2700 mg) were dissolved in 15 mL DMF and heated at 135 °C for 24 h. The purple-colored crystals obtained were washed in DMF and acetone for multiple cycles before drying the powdered material. Post-metalation with Cu of the PCN-222 powder was performed in the presence of $CuCl_2.2H_2O$ (20 mg) dissolved in DMF (18mL) and water (2mL) at a temperature of 100 °C for 24 h. The purple-colored powder turned to brick red, which was then separated, washed with DMF and acetone, and dried prior to electrode preparation. For control studies, the PCN-222 without metalation were used to deposit on the GDE.

Electrode Preparation and Electrochemical Reduction of CO_2: The working electrode was the PCN-222(Cu) catalyst deposition, and the counter electrode for the experiments was Platinum. The detailed catalyst ink preparation and deposition of PCN-222(Cu) on GDE and the fabrication of the flow cell for the electrochemical measurements are included in section S1 (Supporting Information). The catholyte comprised of 0.5 M $TBAPF_6$ dissolved in acetonitrile, while the anolyte was aqueous 0.5 M H_2SO_4 solution. The catholyte and the anolyte chambers were separated by using a pretreated perfluorosulfonic acid-based cation exchange membrane (Nafion 117). Similar suspension was prepared for control studies using PCN-222. All electrochemical experiments were performed in a three-electrode flow cell configuration (Biologic SP300 potentiostat and EC-Lab V11.012 workstation). The operating potentials were referenced versus Ag/AgCl electrode. The ohmic resistance was measured at the open circuit potential by performing electrochemical impedance spectroscopy (EIS) from 100 kHz to 30 Hz before all the experiments and fitted using EC-Laboratory with 85% IR-drop compensation. Prior to the

© 2024 The Author(s). Small published by Wiley-VCH GmbH

16136829, 0, Downloaded from https://onlinelibrary.wiley.com/doi/10.1002/smll.202408010 by University Of Illinois, Wiley Online Library on [29/01/2025]. See the Terms and Conditions (https://onlinelibrary.wiley.com/terms-and-conditions) on Wiley Online Library for rules of use; OA articles are governed by the applicable Creative Commons License

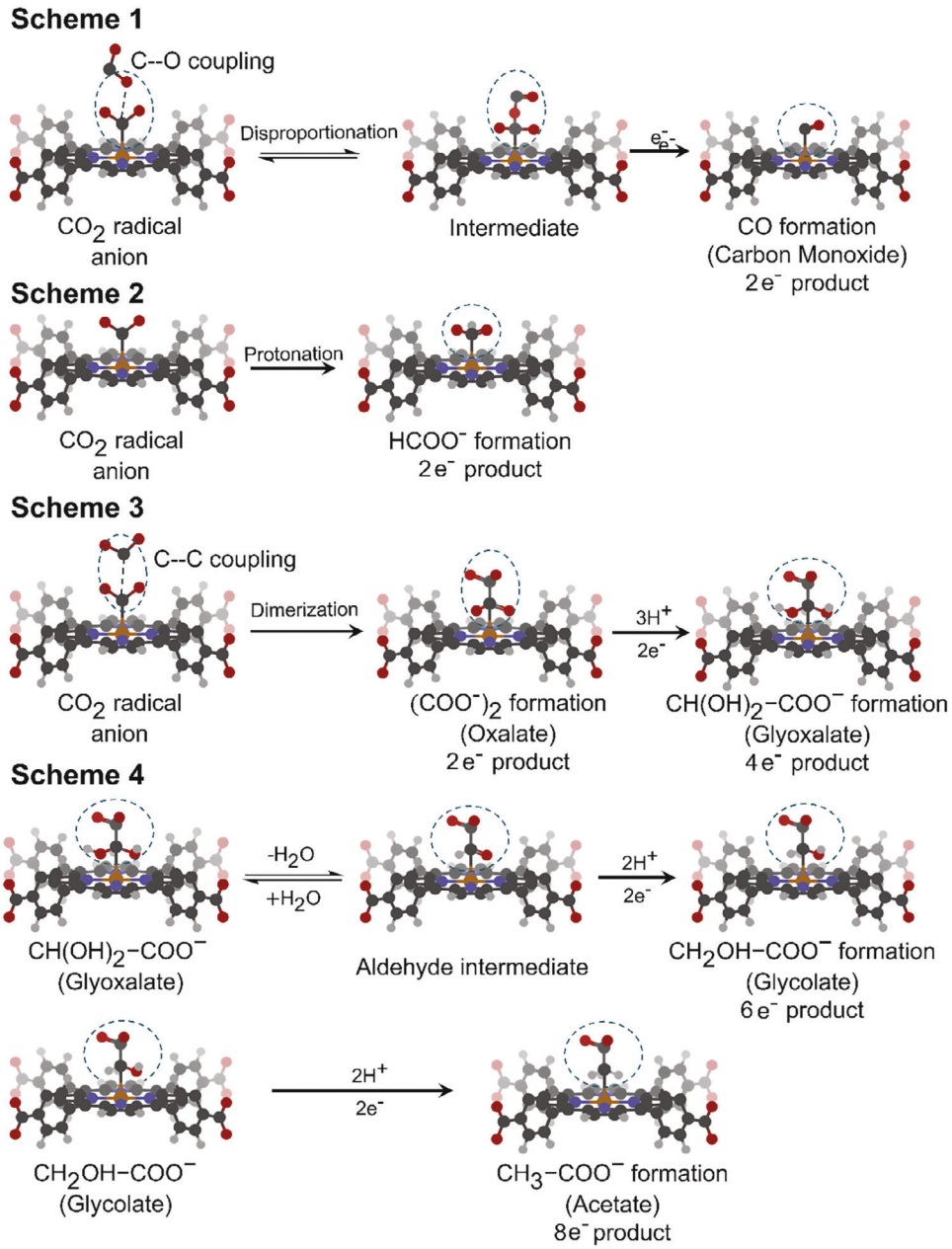

Figure 7. Schemes 1–4 show the different pathways for the formation of CO, formate, oxalate, glyoxalate, glycolate, and acetate.

start of each chronoamperometric experiment, the electrolyte was continuously bubbled with 100% CO_2 for 30 min. During an electrochemical experiment, catholyte was continuously recirculated from a reservoir to the flow cell at 20mL min^{-1} using a peristaltic pump during the experiment.

Characterization of Bulk MOF and Electrodes: Powder & High-resolution X-ray Diffraction XRD were performed on the bulk PCN-222 and thin-film catalyst electrode on GDE respectively, to obtain the signature of the MOF structure and ensure the integrity of the MOF post deposition. SEM coupled with EDS to confirm the crystal morphology and elemental composition of PCN-222(Cu). STEM coupled with EDS was performed to obtain lattice resolution images and the elemental distribution of the PCN-222(Cu) MOF. FTIR was performed as a characterization technique to further confirm the deposition of PCN-222(Cu). XRD and SEM studies were performed for PCN-222 that was utilized as control. FTIR was also used to study the product formation ex situ, after electrochemical reduction of CO_2 at different time intervals. UV spectroscopy was conducted to ensure the loading of single atom Cu in the porphyrin cage. XPS was performed to study the oxidation states and coordination environments of the elements present in PCN-222(Cu), pre- and post-electrolysis. The water content of the post electrolysis samples from the catholyte chamber was measured using KF) titration setup. GC and HPLC were used to measure the gaseous and the liquid products obtained from the CO_2-RR experiments. Detailed information of the characterization and measurement techniques have been provided in Section S2 (Supporting Information).

© 2024 The Author(s). Small published by Wiley-VCH GmbH

16136829, 0, Downloaded from https://onlinelibrary.wiley.com/doi/10.1002/smll.202408010 by University Of Illinois, Wiley Online Library on [29/01/2025]. See the Terms and Conditions (https://onlinelibrary.wiley.com/terms-and-conditions) on Wiley Online Library for rules of use; OA articles are governed by the applicable Creative Commons License

Supporting Information

Supporting Information is available from the Wiley Online Library or from the author.

Acknowledgements

The work was performed in the Materials & Systems Engineering Laboratory at the University of Illinois Chicago. M.R.S. acknowledges funding support from the U.S. National Science Foundation – ECO-CBET program (award no. 2420733) and CMMI (award no. 2326714). This work made use of the NCF facilities and the RRC facilities at UIC. This work also made use of the EPIC and Keck-II facility of Northwestern University's NUANCE Center, which has received support from the SHyNE Resource (NSF ECCS-2025633), the IIN, and Northwestern's MRSEC program (NSF DMR-1720139). This work made use of the IMSERC at Northwestern University, which has received support from the NSF (CHE-1048773 and DMR0521267).

Conflict of Interest

The authors declare no conflict of interest.

Data Availability Statement

The data that support the findings of this study are available in the supplementary material of this article.

Keywords

electrochemical CO_2 reduction, MOF electrocatalysis, non-aqueous electroreduction, single-atom catalyst

Received: September 5, 2024
Revised: November 17, 2024
Published online:

[1] S. Garg, M. Li, A. Z. Weber, L. Ge, L. Li, V. Rudolph, G. Wang, T. E. Rufford, *J. Mater. Chem. A* **2020**, *8*, 1511.
[2] Y. Pei, H. Zhong, F. Jin, *Energy Science & Engineering* **2021**, *9*, 1012.
[3] S. A. Farooqi, A. S. Farooqi, S. Sajjad, C. Yan, A. B. Victor, *Environ. Chem. Lett.* **2023**, *21*, 1515.
[4] Y. Hori, *Modern aspects of electrochemistry*, Springer, Heidelberger Platz **2008**, 89–189.
[5] S. C. Peter, *ACS Energy Lett.* **2018**, *3*, 1557.
[6] G. Centi, S. Perathoner *Green carbon dioxide: advances in CO2 utilization*, John Wiley & Sons, Hoboken, New Jersey **2014**.
[7] S. Jia, X. Ma, X. Sun, B. Han, *CCS Chemistry* **2022**, *4*, 3213.
[8] A. R. Woldu, Z. Huang, P. Zhao, L. Hu, D. Astruc, *Coord. Chem. Rev.* **2022**, *454*, 214340.
[9] J. Zhang, W. Cai, F. X. Hu, H. Yang, B. Liu, *Chem. Sci.* **2021**, *12*, 6800.
[10] N. Jeyachandran, W. Yuan, C. Giordano, *Molecules* **2023**, *28*, 3504.
[11] H. Ait Ahsaine, M. Zbair, A. BaQais, M. Arab, *Catalysts* **2022**, *12*, 450.
[12] D. Wang, J. Mao, C. Zhang, J. Zhang, J. Li, Y. Zhang, *eScience.* **2023**, *3*, 100119.
[13] J. Zhang, C. Guo, S. Fang, X. Zhao, L. Li, H. Jiang, *Nature Communications.* **2023**, *14*, 1298.
[14] G. Zhang, T. Wang, M. Zhang, L. Li, D. Cheng, S. Zhen, Y. Wang, J. Qin, Z.-J. Zhao, J. Gong, *Nat. Commun.* **2022**, *13*, 7768.
[15] X. Wang, K. Klingan, M. Klingenhof, T. Möller, J. Ferreira de Araújo, I. Martens, A. Bagger, S. Jiang, J. Rossmeisl, H. Dau, P. Strasser, *Nat. Commun.* **2021**, *12*, 794.
[16] X. Mei, W. Xu, *Iscience* **2023**, *26*, 108499.
[17] Y. Qian, Y. Liu, H. Tang, B.-L. Lin, *J. CO2 Util.* **2020**, *42*, 101287.
[18] E. Sedano Varo, R. Egeberg Tankard, J. Kryger-Baggesen, J. Jinschek, S. Helveg, I. Chorkendorff, *Journal of the American Chemical Society.* **2024**, *146*, 2015.
[19] H. Da Won, H. Shin, J. Koh, J. Chung, H. Lee, H. Kim, W. SI, *Angew. Chem.* **2016**, *55*, 9297.
[20] A. Goyal, G. Marcandalli, V. A. Mints, M. T. Koper, *J. Am. Chem. Soc.* **2020**, *142*, 4154.
[21] M. Valenti, N. P. Prasad, R. Kas, D. Bohra, M. Ma, V. Balasubramanian, L. Chu, S. Gimenez, J. Bisquert, B. Dam, W. A. Smith, *ACS Catal.* **2019**, *9*, 3527.
[22] Qi Lu, J. Rosen, Y. Zhou, G. S. Hutchings, Y. C. Kimmel, J. G. Chen, F. Jiao, *Nat. Commun.* **2014**, *5*, 3242.
[23] V. Okatenko, A. Loiudice, M. A. Newton, D. C. Stoian, A. Blokhina, A. N. Chen, K. Rossi, R. Buonsanti, *J. Am. Chem. Soc.* **2023**, *145*, 5370.
[24] Y. Jia, F. Li, K. Fan, L. Sun, *Advanced Powder Materials* **2022**, *1*, 100012.
[25] H. Huang, K. Yue, K. Lei, B. Y. Xia, Y. Yan, *J. Phys. Chem. C* **2024**.
[26] E. Plaza-Mayoral, V. Okatenko, K. Dalby, H. Falsig, I. Chorkendorff, P. Sebastián-Pascual, *Iscience* **2024**, *27*, 109933.
[27] Zi-Y Zhang, H. Tian, L. Bian, S-Ze Liu, Y. Liu, Z-Li Wang, *J. Energy Chem.* **2023**, *83*, 90.
[28] G. P. Heim, M. A. Bruening, C. B. Musgrave, W. A. Goddard, J. C. Peters, T. Agapie, *Joule* **2024**, *8*, 1312.
[29] K. Seteiz, J. N. Häberlein, P. A. Heizmann, L. Bohn, S. Vierrath, J. Disch, *ACS Applied Engineering Materials* **2024**, *2*, 1654.
[30] A. T. Bell, *Natl. Sci. Rev.* **2024**, *11*, nwad232.
[31] X. Du, P. Zhang, G. Zhang, H. Gao, L. Zhang, M. Zhang, T. Wang, J. Gong, *Natl. Sci. Rev.* **2024**, *11*, nwad149.
[32] T. Mairegger, H. Li, C. Grießer, D. Winkler, J. Filser, N. G. Hörmann, K. Reuter, J. Kunze-Liebhäuser, *ACS Catal.* **2023**, *13*, 5780.
[33] E. A. dos Reis, G. T. daSilva, E. I. Santiago, C. Ribeiro, *Energy Technol.* **2023**, *11*, 2201367.
[34] A. S. Kumar, M. Pupo, K. V. Petrov, M. Ramdin, J. R van Ommen, W. de Jong, R. Kortlever, *J. Phys. Chem. C* **2023**, *127*, 12857.
[35] V. Sinha, E. Khramenkova, E. A. Pidko, *Chem. Sci.* **2022**, *13*, 3803.
[36] B. Eggins, C. Ennis, R. McConnell, M. Spence, *J. Appl. Electrochem.* **1997**, *27*, 706.
[37] A. C. Garcia, C. Sánchez-Martínez, I. Bakker, E. Goetheer, *ACS Sustainable Chem. Eng.* **2020**, *8*, 10454.
[38] M. König, J. Vaes, D. Pant, E. Klemm, *J. Phys. Chem. C* **2023**, *127*, 18159.
[39] M. König, S.-H. Lin, J. Vaes, D. Pant, E. Klemm, *Faraday Discuss.* **2021**, *230*, 360.
[40] W. Lv, R. Zhang, P. Gao, C. Gong, L. Lei, *J. Solid State Electrochem.* **2013**, *17*, 2789.
[41] H. Sale, G. R. Ubbara, M. D. Symes, *Sustainable Energy Fuels* **2023**, *7*, 5093.
[42] Y. Deng, Y. Wu, G. Chen, X. Zheng, M. Dai, C. Peng, *Chem. Eng. J.* **2021**, *405*, 127004.
[43] O. Shekhah, J. Liu, R. Fischer, C. Wöll, *Chem. Soc. Rev.* **2011**, *40*, 1081.
[44] Q. Qian, P. A. Asinger, M. J. Lee, G. Han, K. Mizrahi Rodriguez, S. Lin, F. M. Benedetti, A. X. Wu, W. S. Chi, Z. P. Smith, *Chem. Rev.* **2020**, *120*, 8161.
[45] C. A. Trickett, A. Helal, B. A. Al-Maythalony, Z. H. Yamani, K. E. Cordova, O. M. Yaghi, *Nat. Rev. Mater.* **2017**, *2*, 1.
[46] R. Saha, K. Gupta, C. J. Gómez García, *Cryst. Growth Des.* **2024**, *24*, 2235.
[47] E. M. Johnson, S. Ilic, A. J. Morris, *ACS Cent. Sci.* **2021**, *7*, 445.
[48] C. Li, L. Zhang, J. Chen, X. Li, J. Sun, J. Zhu, X. Wang, Y. Fu, *Nanoscale* **2021**, *13*, 485.

© 2024 The Author(s). Small published by Wiley-VCH GmbH

16136829, 0, Downloaded from https://onlinelibrary.wiley.com/doi/10.1002/smll.202408010 by University Of Illinois, Wiley Online Library on [29/01/2025]. See the Terms and Conditions (https://onlinelibrary.wiley.com/terms-and-conditions) on Wiley Online Library for rules of use; OA articles are governed by the applicable Creative Commons License

[49] P. K. Verma, C. A. Koellner, H. Hall, M. R. Phister, K. H. Stone, A. W. Nichols, A. Dhakal, E. Ashcraft, C. W. Machan, G. Giri, *ACS Appl. Mater. Interfaces* **2023**, *15*, 53913.
[50] I. Hod, M. D. Sampson, P. Deria, C. P. Kubiak, O. K. Farha, J. T. Hupp, *ACS Catal.* **2015**, *5*, 6302.
[51] X. Xie, X. Zhang, M. Xie, L. Xiong, H. Sun, Y. Lu, Q. Mu, M. H. Rummeli, J. Xu, S. Li, J. Zhong, Z. Deng, B. Ma, T. Cheng, W. A. Goddard, Y. Peng, *Nat. Commun.* **2022**, *13*, 63.
[52] J. Li, C. Chen, L. Xu, Yu Zhang, W. Wei, E. Zhao, Y. Wu, C. Chen, *JACS Au* **2023**, *3*, 736.
[53] M. Velpandian, A. Sinhamahapatra, S. Basu, *Oxford Open Energy* **2023**, *2*, oiad015.
[54] S. A. Chala, K. Lakshmanan, W.-H. Huang, A. W. Kahsay, C-Yu Chang, F. T. Angerasa, Y-Fa Liao, J-Fu Lee, H. Dai, M.-C. Tsai, W.-N. Su, B. J. Hwang, *Applied Catalysis B: Environment and Energy* **2024**, *358*, 124420.
[55] Y. Dai, H. Li, C. Wang, W. Xue, M. Zhang, D. Zhao, J. Xue, J. Li, L. Luo, C. Liu, Xu Li, P. Cui, Q. Jiang, T. Zheng, S. Gu, Y. Zhang, J. Xiao, C. Xia, J. Zeng, *Nat. Commun.* **2023**, *14*, 3382.
[56] C.-H. Gu, S. Wang, Ai-Y Zhang, C. Liu, J. Jiang, H.-Q. Yu, *Proc. Natl. Acad. Sci. USA* **2023**, *120*, 2311585120.
[57] T. Tang, Z. Wang, J. Guan, *Exploration* **2023**, *3*, 20230011.
[58] V. Boor, J. E. Frijns, E. Perez-Gallent, E. Giling, A. T. Laitinen, E. L. Goetheer, L. J. van den Broeke, R. Kortlever, W. de Jong, O. A. Moultos, *Ind. Eng. Chem. Res.* **2022**, *61*, 14837.
[59] J. Feng, S. Zeng, J. Feng, H. Dong, X. Zhang, *Chin. J. Chem.* **2018**, *36*, 961.
[60] G. Li, Y. Liu, Q. Zhang, Q. Hu, W. Guo, X. Cao, Y. Dou, Le Cheng, Y. Song, J. Su, L. Huang, R. Ye, *J. Mater. Chem. A* **2022**, *10*, 19254.
[61] S. Subramanian, K. Athira, M. A. Kulandainathan, S. S. Kumar, R. Barik, *J. CO2 Util.* **2020**, *36*, 105.
[62] N. Hoshi, T. Murakami, Y. Tomita, Y. Hori, *Electrochemistry* **1999**, *67*, 1144.
[63] R. S. Kumar, S. S. Kumar, M. A. Kulandainathan, *Electrochem. Commun.* **2012**, *25*, 70.
[64] B. Bohlen, N. Daems, Z. Su, A. Chen, J. Lipkowski, T. Breugelmans, *ChemSusChem* **2024**, *17*, 202400437.
[65] R. De, S. Gonglach, S. Paul, M. Haas, S. S. Sreejith, P. Gerschel, U.-P. Apfel, T. H. Vuong, J. Rabeah, S. Roy, W. Schöfberger, *Angew. Chem.* **2020**, *132*, 10614.
[66] M. H. Saprudin, P. K. Jiwanti, D. Saprudin, A. R. Sanjaya, Y. M. Putri, Y. Einaga, T. A. Ivandini, *RSC Adv.* **2023**, *13*, 22061.
[67] Li Yang, X. Lv, C. Peng, S. Kong, F. Huang, Yi Tang, L. Zhang, G. Zheng, *ACS Cent. Sci.* **2023**, *9*, 1905.
[68] S. Sarkar, J. Raj, D. Bagchi, A. Cherevotan, C. P. Vinod, S. C. Peter, *EES Catalysis* **2023**, *1*, 162.
[69] Y. Wang, D. Wang, C. J. Dares, S. L. Marquard, M. V. Sheridan, T. J. Meyer, *Proc. Natl. Acad. Sci. USA* **2018**, *115*, 278.
[70] M. Serafini, F. Mariani, A. Fasolini, E. Scavetta, F. Basile, D. Tonelli, *ACS Appl. Mater. Interfaces* **2021**, *13*, 57451.
[71] X.-F. Qiu, J.-R. Huang, C. Yu, Z.-H. Zhao, H.-L. Zhu, Z. Ke, P.-Q. Liao, X.-M. Chen, *Angew. Chem.* **2022**, *134*, 202206470.
[72] Q. Zhu, X. Sun, D. Yang, J. Ma, X. Kang, L. Zheng, J. Zhang, Z. Wu, B. Han, *Nat. Commun.* **2019**, *10*, 3851.
[73] S. Gonglach, S. Paul, M. Haas, F. Pillwein, S. S. Sreejith, S. Barman, R. De, S. Müllegger, P. Gerschel, U.-P. Apfel, H. Coskun, A. Aljabour, P. Stadler, W. Schöfberger, S. Roy, *Nat. Commun.* **2019**, *10*, 3864.
[74] Y. Liu, S. Chen, X. Quan, H. Yu, *J. Am. Chem. Soc.* **2015**, *137*, 11631.
[75] H.-L. Zhu, H.-Y. Chen, Yu-X Han, Z.-H. Zhao, P.-Q. Liao, X.-M. Chen, *J. Am. Chem. Soc.* **2022**, *144*, 13319.
[76] D. Zang, Qi Li, G. Dai, M. Zeng, Y. Huang, Y. Wei, *Appl. Catal., B* **2021**, *281*, 119426.
[77] W. Morris, B. Volosskiy, S. Demir, F. Gańdara, P. L. McGrier, H. Furukawa, D. Cascio, J. F. Stoddart, O. M. Yaghi, *Inorg. Chem.* **2012**, *51*, 6443.
[78] B. L. Bonnett, E. D. Smith, M. de La Garza, M. Cai, J. V. Haag IV, J. M. Serrano, H. D. Cornell, B. Gibbons, S. M. Martin, A. J. Morris, *ACS Appl. Mater. Interfaces* **2020**, *12*, 15765.
[79] C.-W. Kung, T.-H. Chang, Li-Y Chou, J. T. Hupp, O. K. Farha, K.-C. Ho, *Chem. Commun.* **2015**, *51*, 2414.
[80] K. Yu, D.-I. Won, W. I. Lee, W.-S. Ahn, *Korean J. Chem. Eng.* **2021**, *38*, 653.
[81] R. R. Bhawnani, N. K. Dandu, P. K. Podupu, A. T. Ngo, M. R. Singh, *Chem. Mater.* **2024**, *36*, 2402.
[82] A. V. Dighe, L. Huelsenbeck, R. R. Bhawnani, P. Verma, K. H. Stone, M. R. Singh, G. Giri, *JACS Au* **2022**, *2*, 453.
[83] R. R. Bhawnani, R. Sartape, A. Prajapati, P. K. R. Podupu, P. Coliaie, A. N. Nere, M. R. Singh, *J. Membr. Sci.* **2023**, *668*, 121202.
[84] A. Prajapati, N. C. Kani, J. A. Gauthier, R. Sartape, J. Xie, I. Bessa, M. T. Galante, S. L. Leung, M. H. S. Andrade, R. T. Somich, M. V. Rebouças, G. T. Hutras, N. Diniz, M. R. Singh, *Cell Reports Physical Science* **2022**, *3*, 101053.
[85] A. Prajapati, R. Sartape, M. T. Galante, J. Xie, S. L. Leung, I. Bessa, M. H. Andrade, R. T. Somich, M. V. Rebouças, G. T. Hutras, *Energy Environ. Sci.* **2022**, *15*, 5105.
[86] A. Prajapati, R. Sartape, T. Rojas, N. K. Dandu, P. Dhakal, A. S. Thorat, J. Xie, I. Bessa, M. T. Galante, M. H. Andrade, *Energy Environ. Sci.* **2022**, *15*, 680.
[87] J. Shi, T.-Y. Chen, F. Shi, F.-X. Shen, Y.-N. Dai, B. Yang, N. Song, Y.-F. Li, J.-X. Liu, Yu-D Wang, *J. Electrochem. Soc.* **2018**, *165*, G51.
[88] M. Roses, M. Bonet, E. Bosch, *Anal. Chim. Acta* **1996**, *333*, 241.
[89] I. Banik, M. N. Roy, *J. Chem. Eng. Data* **2013**, *58*, 3378.
[90] R. C. Klet, Y. Liu, T. C. Wang, J. T. Hupp, O. K. Farha, *J. Mater. Chem. A* **2016**, *4*, 1479.
[91] W. Liang, X. Wang, W. Yang, S. Zhao, D. Wiley, B. S. Haynes, Y. Jiang, P. Liu, J. Huang, *ACS Cent. Sci.* **2023**, *9*, 27.
[92] R. D. Stern, R. S. Kingsbury, K. A. Persson, *Inorg. Chem.* **2021**, *60*, 15456.
[93] T. J. Zerk, P. V. Bernhardt, *Coord. Chem. Rev.* **2018**, *375*, 173.

© 2024 The Author(s). Small published by Wiley-VCH GmbH

16136829, 0, Downloaded from https://onlinelibrary.wiley.com/doi/10.1002/smll.202408010 by University Of Illinois, Wiley Online Library on [29/01/2025]. See the Terms and Conditions (https://onlinelibrary.wiley.com/terms-and-conditions) on Wiley Online Library for rules of use; OA articles are governed by the applicable Creative Commons License